SCIENCE CHINA
Earth Sciences

•RESEARCH PAPER•

https://doi.org/10.1007/s11430-020-9685-3

Mapping the permafrost stability on the Tibetan Plateau for 2005–2015

Youhua RAN[1,4†], Xin LI[2,3,4*], Guodong CHENG[1,5], Zhuotong NAN[6,7], Jinxing CHE[8], Yu SHENG[1], Qingbai WU[1], Huijun JIN[1], Dongliang LUO[1], Zhiguang TANG[9] & Xiaobo WU[1]

[1] *Northwest Institute of Eco-Environment and Resources, Chinese Academy of Sciences, Lanzhou 730000, China;*
[2] *Institute of Tibetan Plateau Research, Chinese Academy of Sciences, Beijing 100101, China;*
[3] *CAS Center for Excellence in Tibetan Plateau Earth Sciences, Beijing 100101, China;*
[4] *University of Chinese Academy of Sciences, Beijing 100049, China;*
[5] *Institute of Urban Study, Shanghai Normal University, Shanghai 200234, China;*
[6] *Key Laboratory of Virtual Geographic Environment, Ministry of Education, Nanjing Normal University, Nanjing 210023, China;*
[7] *Jiangsu Center for Collaborative Innovation in Geographical Information Resource Development and Application, Nanjing 210023, China;*
[8] *School of Science, Nanchang Institute of Technology, Nanchang 330099, China;*
[9] *National-Local Joint Engineering Laboratory of Geo-Spatial Information Technology, Hunan University of Science and Technology, Xiangtan 411201, China*

Received March 16, 2020; revised August 8, 2020; accepted September 28, 2020; published online November 4, 2020

Abstract Data scarcity is a major obstacle for high-resolution mapping of permafrost on the Tibetan Plateau (TP). This study produces a new permafrost stability distribution map for the 2010s (2005–2015) derived from the predicted mean annual ground temperature (MAGT) at a depth of zero annual amplitude (10–25 m) by integrating remotely sensed freezing degree-days and thawing degree-days, snow cover days, leaf area index, soil bulk density, high-accuracy soil moisture data, and *in situ* MAGT measurements from 237 boreholes on the TP by using an ensemble learning method that employs a support vector regression model based on distance-blocked resampled training data with 200 repetitions. Validation of the new permafrost map indicates that it is probably the most accurate of all currently available maps. This map shows that the total area of permafrost on the TP, excluding glaciers and lakes, is approximately 115.02 (105.47–129.59)×10^4 km^2. The areas corresponding to the very stable, stable, semi-stable, transitional, and unstable types are 0.86×10^4, 9.62×10^4, 38.45×10^4, 42.29×10^4, and 23.80×10^4 km^2, respectively. This new map is of fundamental importance for engineering planning and design, ecosystem management, and evaluation of the permafrost change in the future on the TP as a baseline.

Keywords Mountain permafrost, Third Pole, Remote sensing, Statistical learning

Citation: Ran Y, Li X, Cheng G, Nan Z, Che J, Sheng Y, Wu Q, Jin H, Luo D, Tang Z, Wu X. 2020. Mapping the permafrost stability on the Tibetan Plateau for 2005–2015. Science China Earth Sciences, 63, https://doi.org/10.1007/s11430-020-9685-3

1. Introduction

The Tibetan Plateau (TP), which is also called Earth's "Third Pole", is the highest and most extensive plateau in the world (Yao et al., 2012). The area of high-elevation permafrost on the TP ranks first in the world among middle- and low-latitude permafrost regions, and the permafrost in this region is very sensitive to the increasing warming rate (Pepin et al., 2015). Significant degradation of permafrost in most subregions of the TP has occurred and continues to occur (e.g., Nan et al., 2003; Wu and Zhang, 2008; Yang et al., 2010). Permafrost degradation has resulted in increased environ-

* Corresponding author (email: xinli@itpcas.ac.cn)
† Corresponding author (email: ranyh@lzb.ac.cn)

mental and hazard risks (e.g., Cheng and Wu, 2007; Li et al., 2008; Cheng and Jin, 2013; Wu et al., 2015; Ran et al., 2018). The presence of permafrost and its changes alter or modify soil hydrothermal and biological processes, thereby affecting ecosystem service functions and water systems (e.g., Ye et al., 2004; Cheng and Jin, 2013; Jansson and Taş, 2014). In particular, the degradation of permafrost may affect the stability of infrastructure by reducing the substrate strength and increasing soil permeability, mass movement frequency, thermokarst activity and greenhouse gas fluxes (e.g., Yang et al., 2010; Schuur et al., 2015). Mapping the permafrost on the TP is therefore of critical importance.

Existing maps of permafrost/frozen soil on the TP include the China Map of Snow, Ice, and Frozen Ground (1:4000000) (Shi et al., 1988), the Tibetan Plateau Permafrost Map (1:3000000) (Li and Cheng, 1996), the Circum-Arctic Permafrost and Ground-ice Conditions Map (1:10000000) (Brown et al., 1998), the China Map of Geocryological Regionalization and Classification (1:10000000) (Qiu et al., 2000), the China Map of Glaciers, Frozen Ground and Deserts (1:4000000) (Wang, 2006), and two recently produced permafrost maps that are both derived from a temperature at the top of permafrost (TTOP) model (Zou et al., 2017; Obu et al., 2019). These maps indicate different levels of understanding of the permafrost distribution in different periods, and both contribute to the improvement of permafrost mapping on the TP (Ran et al., 2012). In particular, the accuracy of the latest two maps has been improved by using remote sensing data. However, from the perspective of current knowledge and data accumulation, these existing permafrost maps have two weaknesses. First, the classification systems used in these maps are based on the areal continuity of permafrost, which is defined by the areal fraction of permafrost, except that the map of Zou et al. (2017) provides only the permafrost extent. This was mainly influenced by the system used in both the former Soviet Union and North America, where high-latitude permafrost zones predominate. However, permafrost at high elevations differs substantially from permafrost at high latitudes (Cheng, 1984; Harris et al., 2017). There is an obvious vertical zonation in the distribution of high-elevation permafrost. The vertical projection of so-called "continuous permafrost" on a horizontal plane is usually not continuous but isolated (Cheng, 1984; Harris et al., 2017). Therefore, the continuity-based system is not suitable for describing high-elevation permafrost. In addition, continuity is a relative term and depends on the map scale (Nelson and Outcalt, 1987). This ambiguous definition of continuity and differences in mapping scale may lead to confusion and inconsistency in the mapped distribution of permafrost (Ran et al., 2012). Moreover, traditional permafrost mapping is limited by data scarcity. Global and regional permafrost mapping traditionally relies on *in situ* air temperature measurement data, but meteorological stations are sparse and unevenly distributed on the TP, with compromised representativeness (Li et al., 2020). Only a few stations are distributed in the permafrost regions. The scarcity of such data is an obstacle for high-resolution permafrost mapping.

To address the first weakness, we propose the classification system based on ground thermal stability proposed by Cheng (1984). The system is defined using the mean annual ground temperature (MAGT) at the depth of zero annual amplitude (ZAA) (generally at depths of 10–25 m on the TP), which is one of the most direct and reliable indicators for permafrost occurrence (Romanovsky et al., 2010; Ran et al., 2015). Péwé (1983) considered that this system is workable, and a thermal stability map of North American permafrost based on MAGT was compiled by Harris (1986). First, the thermal stability-based classification system was developed based on the three-dimensional zonation (vertical, latitudinal, and aridity) of high-elevation permafrost; thus, this system considers the differences in the distribution pattern between high-elevation permafrost and high-latitude permafrost, as mentioned in the previous paragraph, and is therefore more suitable for describing high-elevation permafrost than continuity-based systems. Second, ground thermal stability is more closely linked with engineering applications than areal continuity of permafrost. The ground thermal stability reflects the thermal inertia (here, it refers to the energy involved in changing the soil temperature, heat exchange with the external environment, the energy needed to raise the soil temperature and the heat of fusion associated with the ice/water phase change upon thawing/melting or freezing of ground) of permafrost and is related to permafrost degradation stages (Jin et al., 2006; Wu et al., 2010). Understanding the degradation stage of permafrost is vital for engineering planning and design in reducing permafrost-related hazards and for the water cycle, climate change, and ecosystem protection. Third, classification systems based on ground thermal stability are more applicable for grid-based mapping technology, such as GIS and physical-based models, which are commonly used in current permafrost mapping. In grid-based schemes, representing the existence of permafrost is straightforward; however, representing the percentage of permafrost in each grid cell is challenging. Finally, the thermal stability-based definition of permafrost is independent of the map scale. Therefore, it is convenient to evaluate permafrost degradation.

To address the second weakness, remote sensing data and ground-based measurements from multiple sources should be integrated and used. As stated above, air temperature isotherms are usually used to delineate permafrost zones. However, many studies have suggested that air temperature is not a reliable index for permafrost distribution because it neglects the effects of snow cover, vegetation, and other variables, such as surface and thermal offsets, that influence

the occurrence of permafrost (Luo et al., 2018a), which leads to strong spatial heterogeneity even within a small spatial region with consistent topography (Luo et al., 2020). Thus, land surface temperature (LST) should be used instead (Nelson and Outcalt, 1987). Although LST is a relatively reliable criterion, measurements of this quantity are traditionally less readily available than those of air temperature, and its heterogeneity is very strong. Thus, extrapolating LST over regions where such measurements are missing is quite challenging. The rapid development of satellite-based thermal infrared remote sensing technology has changed this situation. Satellite-based measurements of land surface temperature, together with other variables such as snow cover and vegetation structure, with high spatial and temporal resolutions are capable of overcoming the challenges of sparse data faced by permafrost mapping.

This paper aims to develop a new, general and high-resolution permafrost map over the TP based on the ground thermal stability classification system, as proposed by Cheng (1984), by integrating remotely sensed predictor variables, reanalysis data, and ground-measured MAGT using statistical learning technology. A criterion for remotely sensed mean annual land surface temperature (MALST) and land surface frost number (SFN) is also provided to classify permafrost thermal stability. In this section, we have introduced the rationale for thermal stability-based permafrost mapping methods and the objective of this study. Section 2 describes the classification system, methodology, and datasets used in this study. Section 3 presents the results, including the model comparison and accuracy assessment for predicting MAGT, characteristics of permafrost stability on the TP, and remote sensing criteria for mapping permafrost stability. Section 4 discusses the total area of permafrost on the TP and potential applications of the new map. Section 5 summarizes and concludes the paper.

2. Methodology and datasets

2.1 Permafrost classification

Based on the ground temperature survey data along the Qinghai-Tibet Highway and the three-dimensional zonation (vertical, latitudinal, and aridity) of high-elevation permafrost, Cheng (1984) proposed a classification system to describe high-elevation permafrost zonation. This system divided high-elevation permafrost into six types: very stable, stable, semi-stable, transitional, unstable, and very unstable by using the MAGT as the sole indicator. Cheng (1984) also related the thermal stability to permafrost thickness and mean annual air temperature (MAAT) (Table 1). In general, the thermal stability of permafrost is related to the ground temperature and ground ice content. However, until recently, there have been almost no available data on the ground ice content and permafrost thickness across the entire TP. Although the Circum-Arctic Permafrost and Ground-ice Conditions Map provides information on ground ice patterns, its accuracy and spatial resolution are both relatively low (Brown et al., 1998). Ground temperature is still the best indicator for permafrost distribution and is closely related to the thermal stability of permafrost. In addition, the development of many periglacial phenomena is related to the MAGT.

Very unstable permafrost, with MAGT values generally greater than 0°C, occurs on the TP (Cheng, 1984; Nan et al., 2002; Luo et al., 2018a). This refers to cave ice and frozen gravel distributed below the lower limit of permafrost. This type of permafrost is generally relatively thin and is found at either great or shallow depths with a sporadic distribution. It is currently challenging to capture its distribution characteristics at the 1 km scale. Therefore, this type of permafrost was ignored, and the 0°C isotherm of MAGT was used to distinguish permafrost from seasonal frost in this study.

For the temperature index, although only MAAT data are generally available from meteorological stations, MAGT is believed to be a more reliable indicator of permafrost thermal stability. However, due to the high cost and challenge of ground temperature measurements at high elevations, performing finely spaced traditional MAGT measurements is very difficult. With the accumulation of MAGT investigation data and the availability of remote sensing data, it is now possible to estimate MAGT with higher accuracy than in the past.

Table 1 Classification system of high-elevation permafrost[a)]

Type of permafrost based on thermal stability	Classification criteria		
	Mean annual ground temperature (°C)	Thickness of permafrost (m)	Mean annual air temperature (°C)
Very stable	<−5.0	170	<−8.5
Stable	−3.0 to −5.0	110–170	−6.5 to −8.5
Semi-stable	−1.5 to −3.0	60–110	−5.0 to −6.5
Transitional	−0.5 to −1.5	30–60	−4.0 to −5.0
Unstable	0 to −0.5	0–30	−2.0 to −4.0
Very unstable	>0		>−2.0

a) Modified according to Cheng (1984)

2.2 MAGT prediction using a statistical learning model

Ground temperature reaches a point at which its fluctuations exhibit zero amplitude (or within the defined precision of measurements) throughout the year, i.e., the MAGT; this occurs because the ground temperature fluctuations decrease exponentially with increasing depth below the ground surface due to the high thermal inertia of soil (Florides and Kalogirou, 2007). This inertia is related to the physical properties and water/ice state of the soil (Hansson et al., 2004). This air-soil heat balance is also related to snow cover and vegetation cover. Snow cover strongly affects the heat exchange between the soil and the atmosphere due to its high albedo and emissivity in visible light bands, high absorption rate in the infrared and thermal infrared bands, high heat capacity, and low thermal conductivity (Zhang, 2005). The extinction effect of vegetation cover reduces the solar radiation of the ground surface. Therefore, land surface temperature-based indicators including the freezing degree-days (FDD) and thawing degree-days (TDD) (i.e., the annual degree-day totals below and above 0°C, respectively), leaf area index (LAI), snow cover days (SCD), soil moisture, precipitation, soil properties (bulk density, organic content, sand content, silt content, and clay content), and terrain-related factors (elevation and potential incoming solar radiation, PISR) are potential variables (Hachem et al., 2012). In this study, the potential variables mentioned above are optimized and then integrated with *in situ* MAGT measurement data by using a statistical learning model to estimate the MAGT distribution at a 1 km resolution. The flowchart of this process is shown in Figure 1.

2.2.1 Selection of predictor variables using the random forest technique

The random forest technique (Breiman, 2001) is a popular machine learning method. Based on the importance ranking of potential variables and a stepwise ascending variable introduction strategy, it is used for the optimal selection of explanatory variables to build a parsimonious model for MAGT prediction from the potential variables mentioned above. The random forest method involves ensemble means of the predictions from many regression trees. Here, the number of trees is set to 400. Each regression tree is built by using a randomly selected training dataset and five randomly selected predictor variables to split each tree node. The random forest provides two measures for variable selection that include increased mean squared error (%IncMSE) and increased node purity (IncNodePurity). The %IncMSE is used to measure the impact of each variable on model performance. The general idea is to permute the values of each variable and to measure how much the permutation increases the error of the model. IncNodePurity is related to the loss function chosen by the best split. More important variables achieve higher increases in node purities, namely, higher internode variance and smaller intranode variance. For both measures, a variable with a higher value is more important. The main advantage of this technique is the independence from any assumptions regarding the relationships among variables and the distribution of errors, unlike the classical stepwise regression, which is generally based on strong assumptions regarding the functional form of the model (Sandri and Zuccolotto, 2006). The technique is implemented based on the randomForest package in R (Liaw

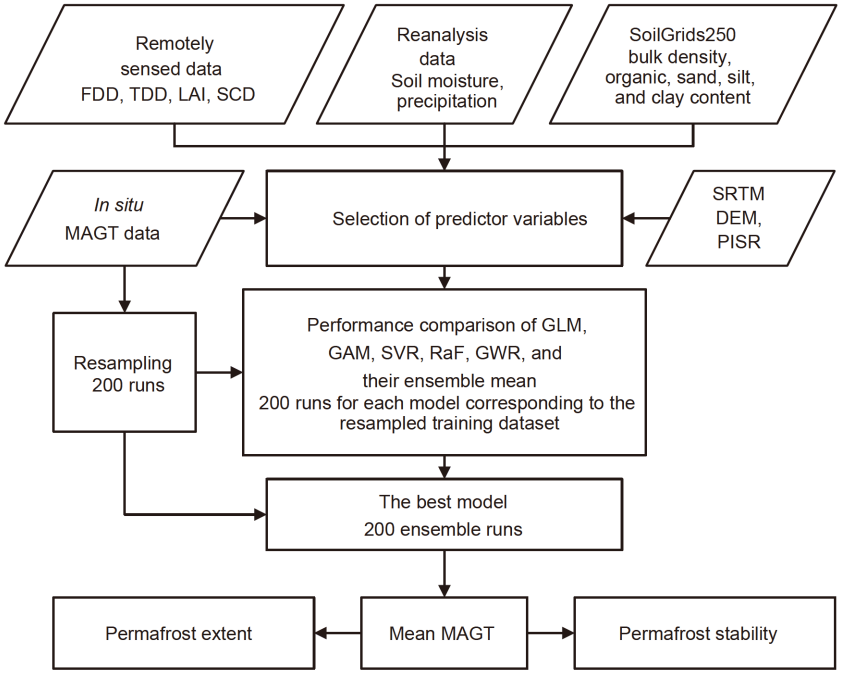

Figure 1 Flowchart of the process used to estimate the MAGT.

and Wiener, 2002).

To reduce the potential overfitting caused by multicollinearity among predictors, the variance inflation factor (VIF) is also used to exclude highly correlated factors. A small VIF (<5) indicates that the multicollinearity of the model is acceptable.

2.2.2 *Statistical learning model*

An optimal model is selected to integrate the observed MAGT and optimally selected predictor for the MAGT prediction by comparing five statistical learning techniques and their ensemble mean. These models are widely used in various regression analyses and include the generalized linear model (GLM) (McCullagh and Nelder, 1989), generalized additive model (GAM) (Hastie and Tibshirani, 1990), support vector regression (SVR) (Vapnik, 1995), random forest (RF) (Breiman, 2001), and geographically weighted regression (GWR) (Brunsdon et al., 1998). To reduce the uncertainty of a single run, the arithmetic mean of 200 runs for each model is used to represent the MAGT distribution in this study. The model in each run is built by using a resampled training dataset (Section 2.3.1). Model performance was assessed based on the root-mean-square error (RMSE), bias, and R squared (R^2) computed by 10-fold cross-validation (CV) with 200 repetitions.

The techniques were implemented based on the R package of mgcv (Wood, 2011) for GLM and GAM, randomForest (Liaw and Wiener, 2002) for RF, e1071 (Karatzoglou et al., 2006) for SVR, and spgwr (Fotheringham, 2002) for GWR. GLM is an extension of the linear model to handle nonlinear relationships for various statistical distributions. Assuming the Gaussian error distribution, GLM was implemented based on first- and second-order polynomials and the identity link function. GAM is a semiparametric extension of GLM that uses a smoothing function to fit nonlinear response curves to the observation (Aalto et al., 2018). In this study, the thin plate regression spline was used as a smoothing function. RF is an ensemble mean of the predictions from many regression trees. Here, the number of trees is set to 500. Each regression tree is built by using a randomly selected training dataset and three randomly selected predictor variables to split each tree node. SVR is a nonparametric technique that attempts to find a function that deviates from observations by a value no greater than a threshold (ε) for each training point while minimizing the prediction error. Its output model depends on kernel functions. Here, the default radial kernel function was used, and the tuning method was used for choosing model parameters. Then, a cost parameter of 1000 was used to avoid overfitting. In GWR, the locally weighted least squares method is used to estimate the parameter values point by point. The Gauss function is used as a spatial weighting function. CV is used to select the optimal bandwidth parameters. For more details on the R package used here, please refer to the relevant documentation (https://cran.r-project.org).

2.3 Datasets and processing

2.3.1 *MAGT ground measurement data*

The MAGT ground measurements at 237 boreholes widely distributed over the TP were integrated mainly from the permafrost monitoring network in China, existing literature (Wu et al., 2007; Yu et al., 2008; Sheng et al., 2010; Li et al., 2011, 2016; Zhang et al., 2011; Sun et al., 2013; Wang et al., 2013; Liu et al., 2015; Qiao et al., 2015; Qin et al., 2017; Cao et al., 2017; Luo et al., 2018b), and some unpublished data. The depths of the MAGT observations are generally greater than 10 m. The elevations of these boreholes range from 3000 to 5300 m, and most of these measurements were made from 2005 to 2015. Their spatial distribution is shown in Figure 2.

To reduce the potential overfitting due to residual autocorrelation, we resampled the training data by excluding sampling points with a distance less than 3 km. This results in an average of 111 measurements used for model training and 12 for model evaluation per CV run.

2.3.2 *Annual freezing and thawing degree-days*

The FDD and TDD (i.e., the annual degree-day totals below and above 0°C, respectively), which are commonly used in permafrost mapping, were derived from daily mean Moderate Resolution Imaging Spectroradiometer (MODIS) LST data. The broad validation indicates that the accuracy of the MODIS LST products is 0.5 K in most cases (Wan et al., 2004). However, cloud contamination is a common problem in optical/thermal satellite data, as clouds hinder LST observations. LST measurements in cloud-covered areas are thus unavailable because cloud-top temperatures are measured in these areas instead (Ackerman et al., 1998). In this study, we used a pragmatic scheme to estimate the daily mean LST based on MODIS LST products (MOD11A1 and MYD11A1 version 5) (four times daily) with 1-km resolution. This scheme assumes that the daily LST amplitude is more homogeneous than the LST itself (Mitchell and Jones, 2005; Liu et al., 2006; Kogan et al., 2011; Ran et al., 2015). The daily mean LST was spatially expanded by interpolating the daily LST amplitude using a gap-filling algorithm. The scheme is easy to implement and has a high computational efficiency. Validation shows that the errors originate primarily from the original MODIS instantaneous LST products. The bias can be removed in the statistical learning model. The workflow of the scheme is shown in Figure 3 and includes the following two primary steps.

Step 1: Enhancing the daily average LST. For pairs of pixels (in which daytime and nighttime data are both available on particular days), the daily average LST is calculated

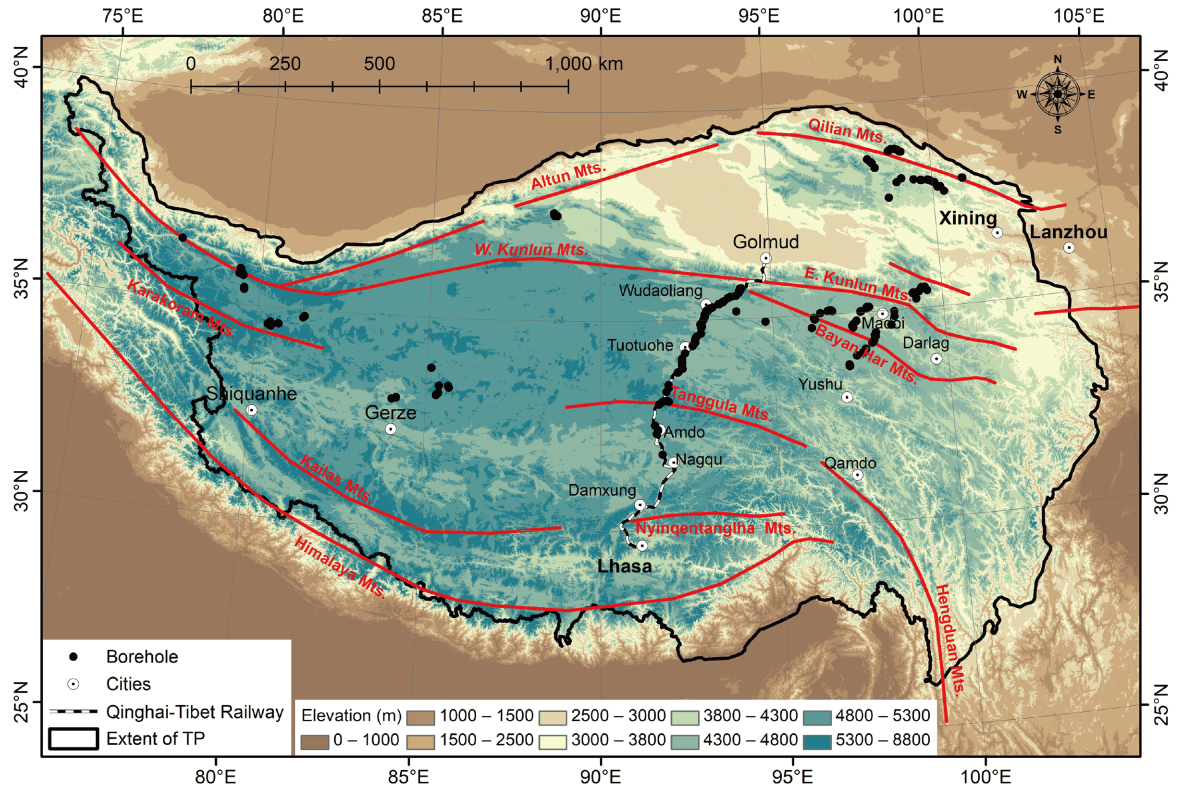

Figure 2 Distribution of boreholes for ground temperature measurement across the Tibetan Plateau.

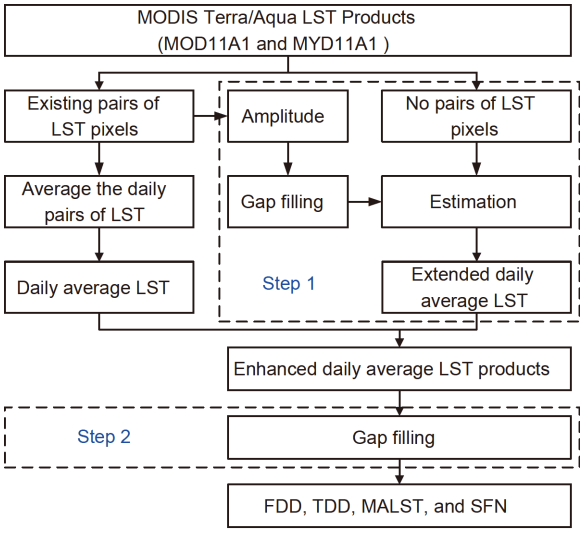

Figure 3 The workflow used to estimate annual freezing degree-days (FDD) and thawing degree-days (TDD), mean annual land surface temperature (MALST), and surface frost number (SFN).

as the arithmetic average of the daytime and nighttime LSTs. The LST amplitude for the day and pixel in question is also obtained. We interpolate the LST amplitude to the entire TP using a gap-filling procedure (see Step 2), and this field is used to estimate the daily average LST values for pixels where pairs are not available (i.e., either the daytime or nighttime data are not available on a certain day, but at least one of these values is available). Finally, the enhanced daily average LST is generated by combining the daily average LST for pairs of pixels and the extended daily average LST for unpaired pixels (Figure 3).

Step 2: Gap-filling for enhanced daily average MODIS LSTs. Although the daily average LSTs can be enhanced, there are always many missing and low-quality values in the data. In this step, the missing values are estimated by implementing a gap-filling procedure that uses a robust smoothing algorithm, i.e., penalized least square regression based on discrete cosine transforms (DCT), which explicitly utilizes time-series information to estimate missing values (Garcia, 2010). For mathematical details of the robust smoothing algorithm, refer to Garcia (2010).

Using the above algorithm, the 1-km daily mean MODIS LSTs over the TP from January 1, 2005, to December 31, 2015, were produced. Then, multiyear mean values of FDD, TDD, MALST, and SFN from 2005 to 2015 are calculated. FDD and TDD were used as potential predictor variables to estimate MAGT. MALST and SFN were used to define the criterion to classify permafrost stability. In this study, the SFN is calculated using Eq. (1) (Nelson and Outcalt, 1987).

$$\mathrm{SFN} = \frac{\mathrm{FDD}^{1/2}}{\mathrm{FDD}^{1/2}+\mathrm{TDD}^{1/2}}, \quad (1)$$

where the FDD and TDD are derived from the daily average LST.

2.3.3 *Snow, vegetation and soil data*

Identical to the process used by Ran et al. (2018), based on two high-quality datasets that include a daily cloud-removed snow cover fraction product derived from a MODIS snow cover product (MOD10A1) with 1-km resolution based on the cubic spline interpolation algorithm (Tang et al., 2013) and Global Land Surface Satellite (GLASS) 1-km LAI product (Xiao et al., 2014; Xiang et al., 2014), the mean SCD and LAI during 2005 to 2014 were calculated and used in this study. The SCD is the total number of days that a pixel is covered with snow in a year, which is calculated based on the cloud-free daily snow cover fraction products. Only the pixels with snow cover fractions greater than 50% are considered snow-covered pixels.

The soil properties from SoilGrids250, including organic content, clay content, silt content, sand content, and bulk density, were used. SoilGrids250 is a global gridded soil map with a spatial resolution of 250 m that is derived from 150000 soil profiles around the world and 158 remote sensing-based soil environmental covariates based on machine learning algorithms. It was developed by the International Soil Reference and Information Center (ISRIC) as part of the World Soil Information (WSI) within the Global Soil Information Facilities (GSIF) framework as a result of broad international collaboration (Hengl et al., 2017). The soil properties over the TP at seven standard depths (0, 5, 15, 30, 60, 100 and 200 cm) can be freely downloaded from www.SoilGrids.org, and the mean values of each property at each of these depths were used in this study.

2.3.4 *Reanalysis data*

The high-quality soil moisture dataset used in this study was obtained from the Climatic Data Center, National Meteorological Information Center, China Meteorological Administration (CMA). The dataset is the result of a multimodel ensemble prediction system developed by the CMA based on the Community Land Model (CLM 3.5) of the US National Center for Atmospheric Research (NCAR), the Common Land Model (CoLM), the Noah-MP1-4 model, and high-quality atmospheric forcing datasets that fuse data from the FY2 geostationary meteorological satellite with intensive ground observations collected at approximately 40000 automatic weather stations in China (Shi et al., 2011; Shen et al., 2014). Validation shows that the product reflects the temporal-spatial distribution of soil moisture reasonably well. The correlation coefficient, RMSE, and bias values are 0.89, 0.02 $m^3\ m^{-3}$, and 0.02 $m^3\ m^{-3}$, respectively. The spatial resolution of this product is 6 km, and its temporal resolution is 1 h. The annual mean soil moisture estimates extending from 2008 to 2010 at five depths (5, 10, 40, 80, and 200 cm) over the TP were used in this study. Precipitation, which is a component of the high-quality atmospheric forcing datasets, was used directly in this study.

2.3.5 *Terrain data*

Two terrain-related variables, the digital elevation model (DEM) and topography-derived PISR, were used in this study. PISR was computed using the method proposed by McCune and Keon (2002) based on a remotely sensed DEM, i.e., the National Aeronautics and Space Administration (NASA) Shuttle Radar Topographic Mission (SRTM) DEM with a 1-km spatial resolution.

2.3.6 *Ancillary data*

To maintain the consistency of the lake distribution with the environmental variables mentioned above, the water body distribution from the MODIS land cover product (MOD12Q1) and the glacier extent from the second Chinese glacier inventory (Guo et al., 2015) were used as masks to support the statistics of the permafrost area.

2.4 Accuracy assessment

2.4.1 *Assessment of predicted MAGT*

Three methods were used to evaluate the accuracy of the predicted MAGT. First, the RMSE, bias, and coefficient of determination (R^2) were used to assess the performance of the candidate model. These indexes were computed by distance-blocked 10-fold CV with 200 repetitions. Second, following Aalto et al. (2018), the uncertainty of the predicted MAGT was assessed by using two percentile indexes, median uncertainty (PI50) and the 95th percentile uncertainty (PI95), which were calculated according to the percentile intervals (PI, 97.5th–2.5th percentile) of ensemble simulated MAGT over the TP. Third, extended triple collocation (ETC) was used to investigate the relative error of the predicted MAGT. Triple collocation (TC) is a powerful tool for estimating the unknown RMSE for three of the same geophysical variables retrieved using mutually independent methods (Zwieback et al., 2012). It has been successfully applied to the validation of remote sensing products and simulation results (Fang et al., 2012; Dorigo et al., 2015). McColl et al. (2014) extended the TC technique by deriving an additional index, i.e., the correlation coefficient of the estimated result with respect to an unknown "truth". This metric provides a complementary expression for the uncertainty of a simulation result by integrating the sensitivity of the simulation result with the unknown "true" value, measurement noise, and variability of the variable itself (McColl et al., 2014).

We assume that the "true" MAGT value t and the three measurements of MAGT can be represented as follows:

$$Y_i = a_i + b_i t + \varepsilon_i, \quad (2)$$

where Y_i ($i \in \{1, 2, 3\}$) represents the three measurements of MAGT, which are linearly related to t with additive random errors ε_i. In this study, the three MAGT measurements include the predicted MAGT, *in situ* MAGT measurements obtained at 237 boreholes, and the MAGT values predicted by the improved Noah land surface model (Wu et al., 2018). The Noah model is selected mainly because of its improvement in data and physical processes, and it may have higher accuracy. According to the situation of the TP, the Noah model features improvements in the thermal roughness scheme for sparse vegetation, the thermal conductivity scheme for gravel, and the hydraulic conductivity scheme for the impedance of soil water flow. The improved model was examined and applied to model the MAGT at ZAA on the TP using subsurface soil compositions, i.e., a new 18-layer soil dataset with a total depth of 15.2 m. This 18-layer, 15.2-m-deep simulation corresponded to the availability of soil data (Wu et al., 2018).

The RMSE, i.e., the variance in the residual errors ε_i for each data set, can be obtained by using the TC estimation equation:

$$\sigma_\varepsilon = \begin{bmatrix} \sqrt{\mathrm{Cov}(Y_1, Y_1) - \dfrac{\mathrm{Cov}(Y_1, Y_2)\mathrm{Cov}(Y_1, Y_3)}{\mathrm{Cov}(Y_2, Y_3)}} \\ \sqrt{\mathrm{Cov}(Y_2, Y_2) - \dfrac{\mathrm{Cov}(Y_1, Y_2)\mathrm{Cov}(Y_2, Y_3)}{\mathrm{Cov}(Y_1, Y_3)}} \\ \sqrt{\mathrm{Cov}(Y_3, Y_3) - \dfrac{\mathrm{Cov}(Y_1, Y_3)\mathrm{Cov}(Y_2, Y_3)}{\mathrm{Cov}(Y_1, Y_2)}} \end{bmatrix}, \quad (3)$$

where $\mathrm{Cov}(Y_i, Y_j)$ is the covariance between the different MAGT measurements.

The correlation coefficient of the three MAGT measurements with respect to the unknown "true" MAGT values can be obtained by using the ETC estimation equation:

$$r_{t,Y} = \begin{bmatrix} \sqrt{\dfrac{\mathrm{Cov}(Y_1, Y_2)\mathrm{Cov}(Y_1, Y_3)}{\mathrm{Cov}(Y_1, Y_1)\mathrm{Cov}(Y_2, Y_3)}} \\ \mathrm{Cov}(Y_1, Y_3)\mathrm{Cov}(Y_2, Y_3)\sqrt{\dfrac{\mathrm{Cov}(Y_1, Y_2)\mathrm{Cov}(Y_2, Y_3)}{\mathrm{Cov}(Y_2, Y_2)\mathrm{Cov}(Y_1, Y_3)}} \\ \mathrm{Cov}(Y_1, Y_2)\mathrm{Cov}(Y_2, Y_3)\sqrt{\dfrac{\mathrm{Cov}(Y_1, Y_3)\mathrm{Cov}(Y_2, Y_3)}{\mathrm{Cov}(Y_3, Y_3)\mathrm{Cov}(Y_1, Y_2)}} \end{bmatrix}. \quad (4)$$

2.4.2 *Assessment of permafrost extent*

We validated the predicted permafrost extent by comparing it with existing permafrost maps or investigation data at three different scales. At the site scale, 237 boreholes (34 in the zone of seasonal frost) were used to validate the different permafrost maps covering the TP at the site scale to determine whether the accuracy of the permafrost map obtained in this study is higher than those reflected by the other maps, i.e., Li and Cheng (1996), Nan et al. (2002), and Zou et al. (2017). The updated permafrost distribution along the Qinghai-Tibet Highway and Railway (QTR map) was used at the local scale. At the regional scale, three permafrost distribution maps over the TP from Li and Cheng (1996), Nan et al. (2002), and Zou et al. (2017), providing representative results from different periods, were used at the regional scale. In particular, the map of Zou et al. (2017) integrated the MODIS eight-day LST product using the TTOP model and careful validation using ground investigation data.

3. Results

3.1 Variables for MAGT prediction

Combined with the importance ranking of 13 potential predictor variables based on %IncMSE, IncNodePurity, multicollinearity analysis, and empirical judgment, seven variables, including FDD, TDD, LAI, SCD, elevation, soil moisture, and soil bulk density, are selected to estimate MAGT (Figure 4). %IncMSE and IncNodePurity generally reflect the importance of the potential predictor variables, which is consistent with our understanding for air-soil heat balance mentioned in Section 2.2, except for SCD probably due to the spatial representativeness of the samples. There are few borehole samples in the key snow cover area. FDD and TDD, as representative of the climate conditions, are commonly used to map permafrost (Nelson and Outcalt, 1987; Aalto et al., 2018). The importance of elevation for MAGT prediction is also well understood for permafrost on the TP due to the altitudinal dependence of climate and local ecosystem conditions, but the relationship is complex (Li and Cheng, 1999). The importance of soil bulk density and soil moisture content is well known to influence soil thermal conductivity (Nelson and Outcalt, 1987). For the importance of soil sand content and SCD, SCD was selected here based on the understanding of its important influence on the soil-atmosphere energy balance, as mentioned in Section 2.2. For the seven variables selected here, the VIF is less than 5.

Although the statistical selection of predictor variables may be affected by the uncertainty inherited with the data used in this study, its consistency with previous knowledge shows that the training sampling used in this paper can capture the main factors controlling or influencing the distribution of ground temperature.

3.2 Model performance for predicting MAGT

CV of 200 runs shows that the five statistical learning techniques (GLM, GAM, SVR, RF, and GWR) and their ensemble mean all achieved high accuracy. Except for the GAM, the techniques showed no significant difference in predictions. However, the mean values of the three statistical indicators, i.e., RMSE, bias, and R^2, show that the ensemble mean is more accurate than any single model, although SVR yielded a predictive performance similar to that of the en-

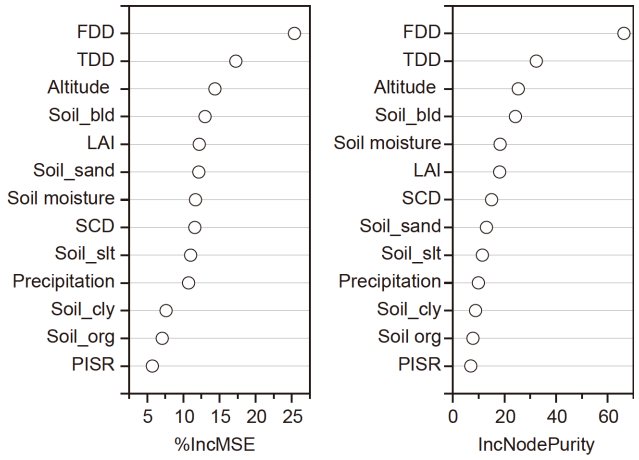

Figure 4 The importance ranking of potential predictors used to estimate MAGT based on the random forest method. IncMSE, increased mean squared error. IncNodePurity, increased node purity.

semble mean of the five models (RMSE=0.75°C, bias =0.01°C, R^2=0.71; Table 2). Therefore, SVR was used to estimate the MAGT in this study.

The predicted MAGT and the corresponding distribution of permafrost thermal stability over the TP were generated based on 200 runs of the SVR model, as shown in Figures 5 and 6. The median uncertainty (PI50) and 95th percentile uncertainty (PI95) of the predicted MAGT are ±0.65°C and ±2.25°C over the TP, respectively. This uncertainty indicates that the low instability of the SVR model may come from ground measurement data of MAGT and predictor variables. The map shows the detailed distribution of permafrost on the TP. The specific distribution characteristics are described in Section 3.3. The assessment of relative accuracy can be found in Section 3.4.

3.3 Permafrost distribution characteristics on the TP

3.3.1 General distribution characteristics of permafrost

This map shows that the total area of permafrost, excluding glaciers and lakes, is approximately 115.02×10^4 km^2. The areal extents of very stable, stable, semi-stable, transitional, and unstable types are 0.86×10^4, 9.62×10^4, 38.45×10^4, 42.29×10^4, and 23.80×10^4 km^2, respectively (Table 3). These results indicate that the transitional type dominates the permafrost region on the TP. The total areas occupied by permafrost in the Tibet Autonomous Region, Qinghai Province, Xinjiang Uygur Autonomous Region, Sichuan, Gansu and Yunnan provinces are 52.13×10^4, 34.45×10^4, 21.85×10^4, 3.66×10^4, 2.73×10^4, and 0.21×10^4 km^2, respectively. In the Tibet Autonomous Region, Qinghai, and Gansu provinces, permafrost is dominated by transitional permafrost. The Xinjiang Uygur Autonomous Region and Sichuan Province are dominated by the semi-stable and unstable types, respectively.

Overall, the very stable and stable permafrost types are mainly distributed in high mountains, especially in the Qilian, West Kunlun mountains, and Karakoram mountains. The semi-stable permafrost, along with the lower limit of the stable permafrost type, is mainly found in the Qiangtang Plateau, West Kunlun, and Qilian Mountains. The transitional type is mainly distributed along the Qinghai-Tibet Railway and in the source area of the Yellow River. Finally, unstable permafrost is mainly distributed in the southern part of the Qiangtang Plateau, along the Qinghai-Tibet Railway and in the eastern part of the Three Rivers Headwaters region.

3.3.2 Elevation and aspect characteristics of permafrost thermal stability

Figure 7 shows the permafrost area and the fractions of different stability types along with elevation and aspect (i.e., north-facing and south-facing slopes) on the TP. Permafrost occurs above 2000 m above sea level (asl) and is mainly distributed between 4000–5500 m, with a peak at approximately 5000 m. Permafrost below 4000 m accounts for approximately 8.2% of the total permafrost on the TP (Figure 7a). The thermal stability of permafrost on the TP increases with increasing elevation. The mean elevations of the very stable, stable, semi-stable, transitional, and unstable types are 5497, 5189, 4967, 4767, and 4612 m asl, respectively. More than 90% of the very stable, stable, semi-stable, transitional, and unstable permafrost types are distributed above 3700, 4000, 4200, 4500, and 4900 m asl, respectively (Figure 7b–7f).

The altitudinal variations in permafrost distribution are also dependent on aspect. Figure 7 shows that the aspect mainly acts on the permafrost distribution below 5100 m asl, where the area of permafrost developed on north-facing slopes is larger than that on south-facing slopes because north-facing slopes likely receive less solar radiation than south-facing slopes. Above 5100 m asl, elevation controls

Table 2 . The predictive performance of mean annual ground temperature (MAGT) for five statistical models and their ensemble mean[a)]

Performance measures	GLM	GAM	SVR	RF	GWR	Ensemble
RMSE (°C)	0.76±0.20	0.81±0.26	0.75±0.21	0.78±0.20	0.77±0.22	0.75±0.20
Bias (°C)	0.00±0.23	0.01±0.26	0.01±0.22	0.00±0.25	–0.01±0.23	0.00±0.23
R^2	0.70±0.15	0.68±0.16	0.71±0.15	0.69±0.15	0.69±0.17	0.71±0.15

a) GLM, generalized linear model; GAM, generalized additive model; SVR, support vector regression; RF, random forest; GWR, geographically weighted regression. RMSE, bias, and R^2 with 1 standard deviation

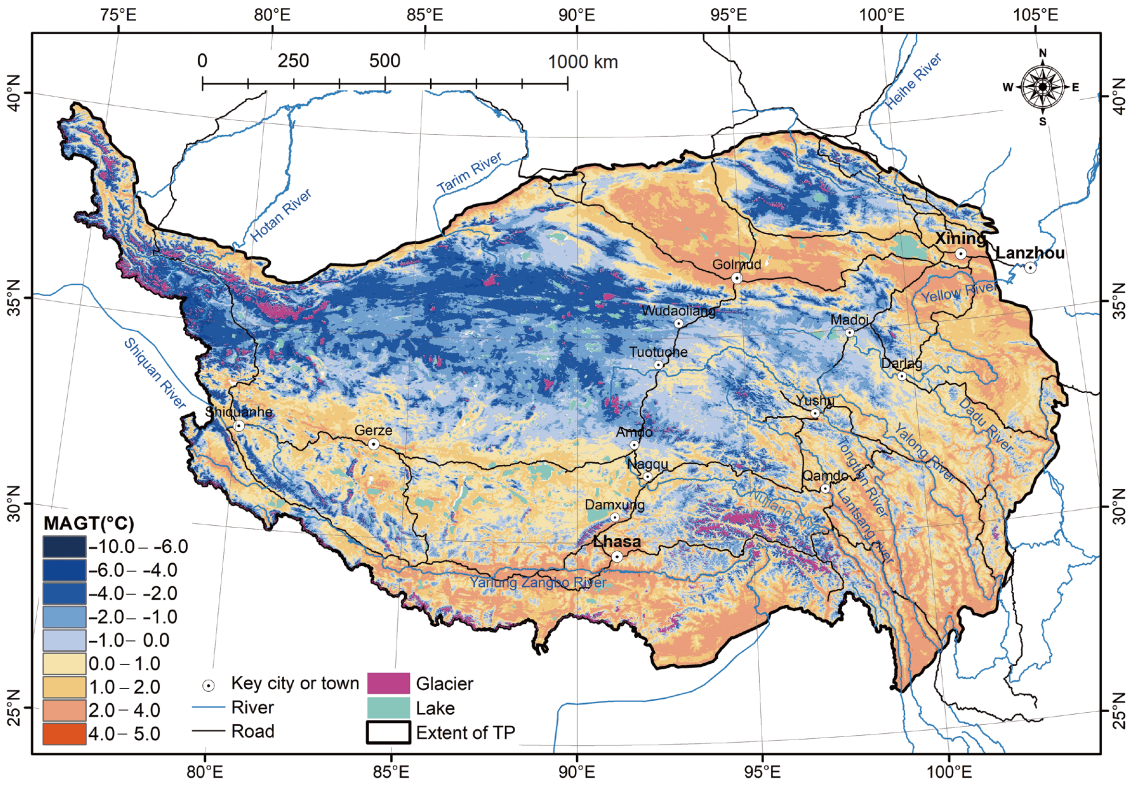

Figure 5 Map of predicted mean annual ground temperature (MAGT) on the Tibetan Plateau.

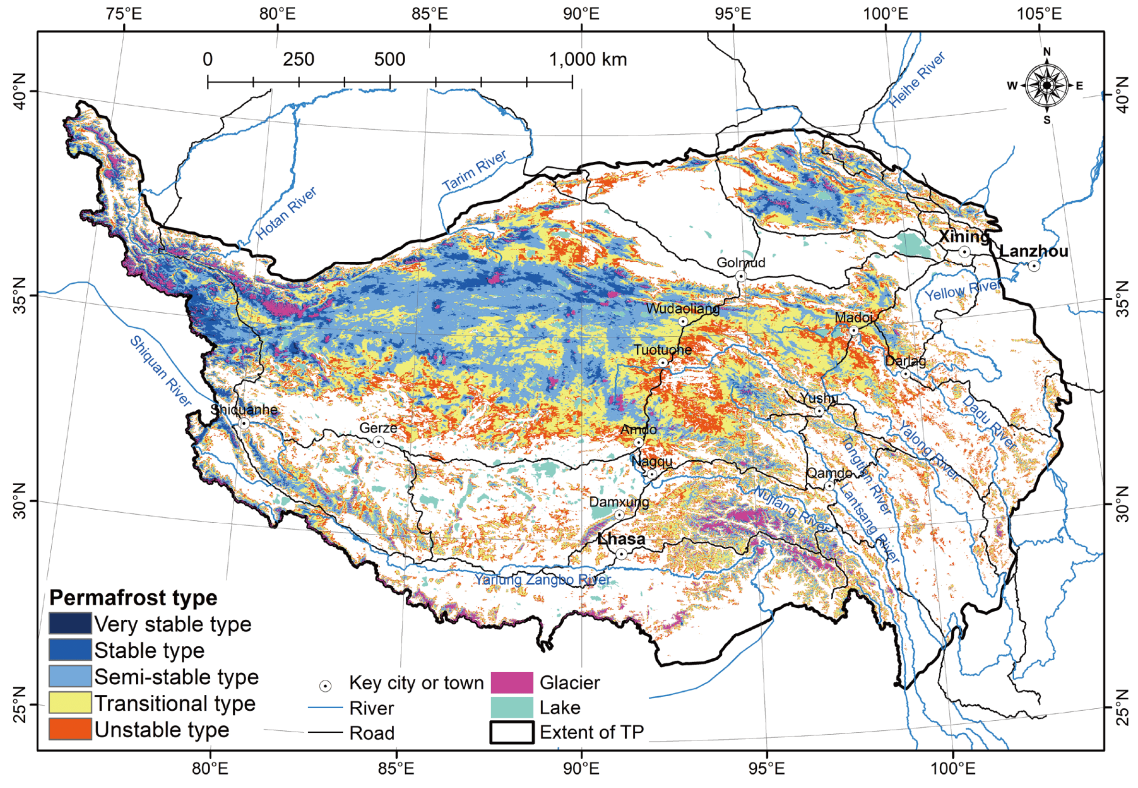

Figure 6 Map of the thermal stability of permafrost on the Tibetan Plateau.

the permafrost distribution. In general, the fraction of permafrost on north- and south-facing slopes accounts for 48.7% and 46.3%, respectively, and the remainder is distributed in flat terrain (Figure 7b–7f). Additionally, the alti-

Table 3 Areal extents of permafrost thermal stability types in different administrative regions on the Tibetan Plateau[a)]

Stability type	Tibet ($\times10^4$ km^2)	Qinghai ($\times10^4$ km^2)	Xinjiang ($\times10^4$ km^2)	Sichuan ($\times10^4$ km^2)	Gansu ($\times10^4$ km^2)	Yunnan ($\times10^4$ km^2)	Total area ($\times10^4$ km^2)
Very stable	0.16	0.04	0.65	0.00	0.01	0.00	0.86
Stable	3.07	1.66	4.68	0.01	0.21	0.00	9.62
Semi-stable	18.27	10.14	8.84	0.28	0.92	0.00	38.45
Transitional	19.77	14.76	5.23	1.50	0.95	0.08	42.29
Unstable	10.86	7.85	2.46	1.88	0.64	0.12	23.80
Total area	52.13	34.45	21.85	3.66	2.73	0.21	115.02

a) Excluding glaciers and lakes

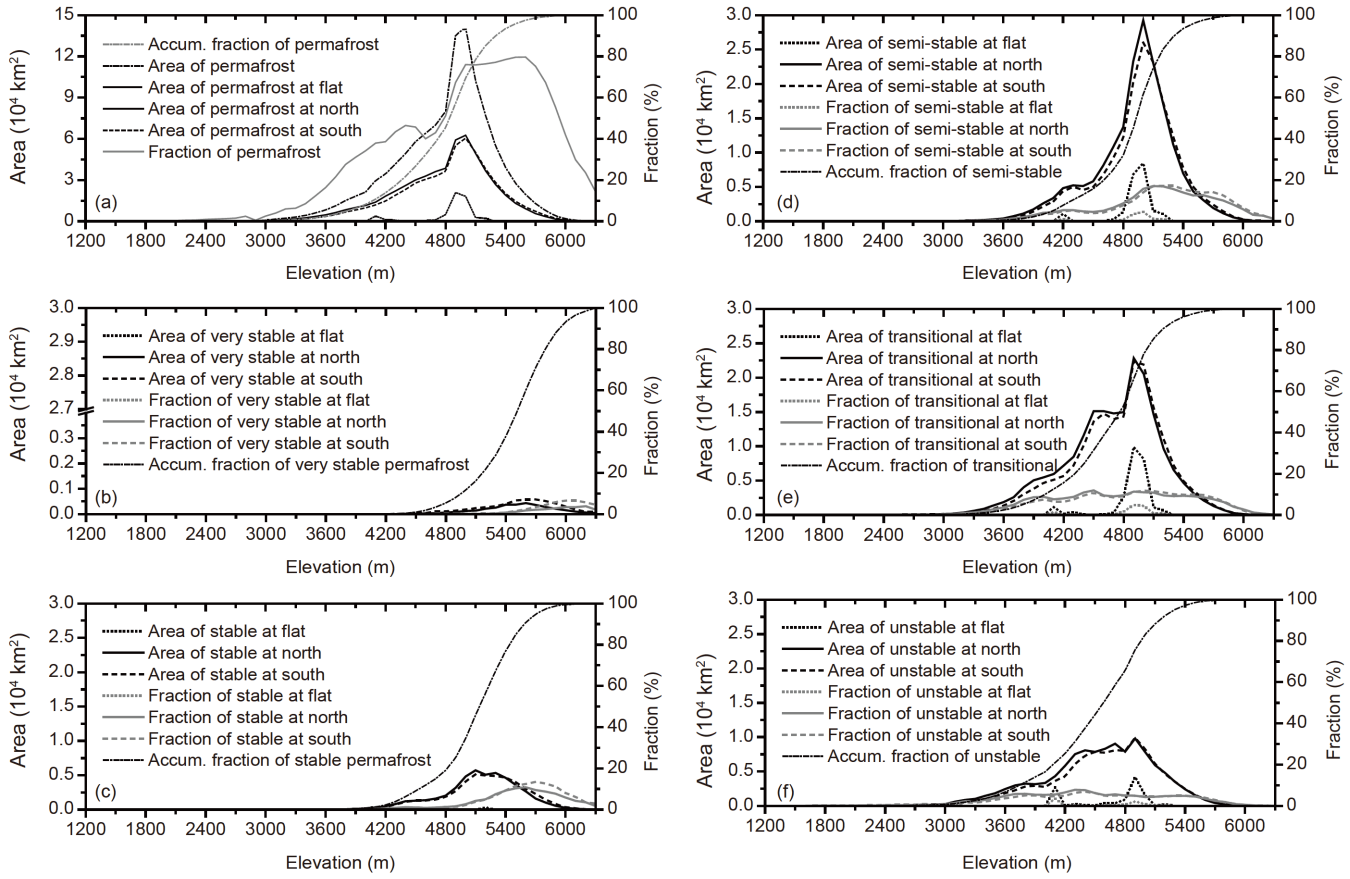

Figure 7 The permafrost area and the fractions of different stability types in each elevation interval and the accumulated fraction with elevation on the Tibetan Plateau.

tudinal dependence of the permafrost distribution is also related to latitude and longitude, but these factors have a relatively weak influence. In a similar elevation range, the permafrost at high latitudes has a higher stability level, which is relatively obvious on the Qiangtang Plateau.

3.3.3 Permafrost stability along the Qinghai-Tibet Railway

The Qinghai-Tibet Railway is a major engineering corridor. According to the new maps proposed in this study, along the 10-km-wide engineering corridor of the Qinghai-Tibet Railway from Golmud to Lhasa (with a total length of approximately 1118 km), the permafrost area accounts for 58.43% of this region and is dominated by semi-stable, transitional, and unstable permafrost types. The areas (and proportions) of the semi-stable, transitional and unstable permafrost types are 1185 (10.8%), 3497 (31.87%), and 1650 km^2 (15.4%), respectively.

3.4 Relative accuracy

3.4.1 Relative accuracy of the predicted MAGT

The comparison of RMSE and correlation coefficients estimated by using ETC (eqs. (3) and (4)) for the MAGT from

borehole measurements, the output of the Noah land surface model, and the predicted result of this study show that the RMSE for the predicted MAGT in this study is the lowest, and the squared correlation coefficient is the highest (Figure 8). These results indicate that the uncertainty in the predicted MAGT in this paper may be the smallest with respect to the unknown "true" MAGT at the grid scale. The larger uncertainty in the ground MAGT measurement than in the predicted MAGT is probably due to the greater spatial representativeness error of the *in situ* measurements at the grid scale, while the grid-based model reduces the representativeness error by considering grid-scale heterogeneity (Li, 2014).

Although it exhibits the smallest residual error variance and the highest squared correlation coefficient, the predicted MAGT in this paper still includes some potential uncertainties. These uncertainties mainly arise from the representativeness of the borehole locations and the potential error of predictor variables. First, although the MAGT measurements at the 237 boreholes were integrated into the modeling process and this number of measurements is greater than those used in any previous study, these boreholes are mainly distributed in relatively low-elevation areas, and measurements in high-elevation regions are still generally unavailable. A broader scientific challenge involving more accurately simulating the MAGT requires further data accumulation and optimization of the observational network design to improve the spatial representativeness of borehole data at both the grid scale and the TP scale.

3.4.2 *Relative accuracy of permafrost extent*

The comparison of permafrost distribution at the three different scales studied here shows that the permafrost distribution produced by this study is more accurate and reasonable than those produced by previous maps. At the site scale, 84% of the 237 boreholes examined are consistent with the map of this study, while the proportions in the maps of Li and Cheng (1996), Nan et al. (2002), and Zou et al. (2017) exhibit consistencies of only 68%, 28%, and 81%, respectively. At the local scale, as shown in Figure 9e, the permafrost distribution obtained by this study is very close to that in the QTR map. At the regional scale, this comparison shows that the patterns of permafrost distribution are generally similar among the three maps of permafrost distribution on the TP (Li and Cheng, 1996; Nan et al., 2002; Zou et al., 2017). The differences are small, especially when the results of this study are compared with the new permafrost distribution map developed by Zou et al. (2017). As shown in Figure 9a–d, the main differences exist within four regions, including the region of Gerze, west of the Kailas Range, the region to the east of Lhasa, and the eastern TP. The differences relative to Nan's map in the region of Gerze and the region to the east of Lhasa are mainly derived from the uncertainty associated with Nan's map because the permafrost distribution in this map was based on MAGT measurements obtained from just 76 sites along the QTR and a DEM. In the region of Gerze, recent surveys have shown that the lower limit of permafrost lies farther north than that derived from the published permafrost map (Nan et al., 2013; Ran et al., 2018). This survey indicates that the permafrost distributions in this study and Zou et al. (2017) are more accurate than those in previous maps. In the region east of Lhasa, where glaciers and snow cover are present, no survey data are currently available. However, permafrost distribution may be underestimated by the elevation-based MAAT or MAGT interpolation method used for previous maps (Li and Cheng, 1996; Nan et al., 2002) because the average elevation of this region is relatively low but the temperature is low (Ran et al., 2015; Ran et al., 2018). The permafrost extent in this study is very similar to the latest results presented in Zou et al. (2017) for this region. In the eastern region of the TP, two recent surveys in the Bayan Har Mountains by Luo et al. (2018b) and Zou et al. (2017) both showed that the extent of permafrost was overestimated by Li and Cheng (1996).

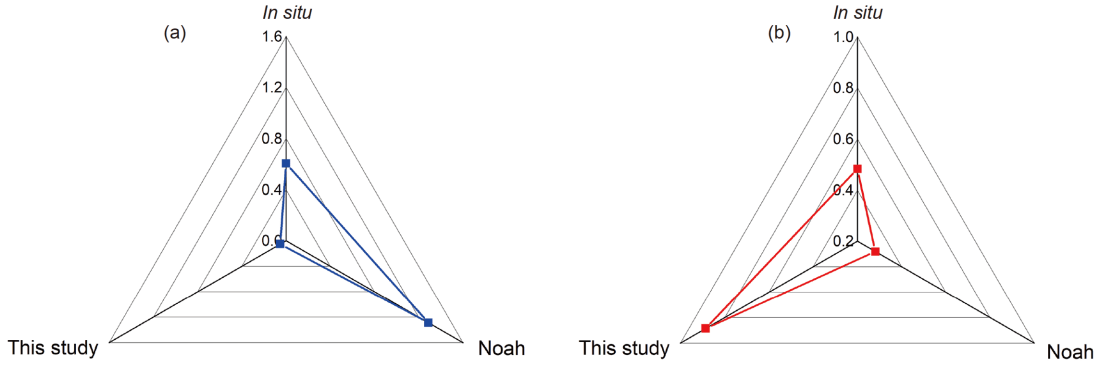

Figure 8 The RMSE (a) and correlation coefficient (b) estimated by using extended triple collocation for *in situ* borehole MAGT measurements, the MAGT output of the Noah land surface model, and the predicted MAGT of this study.

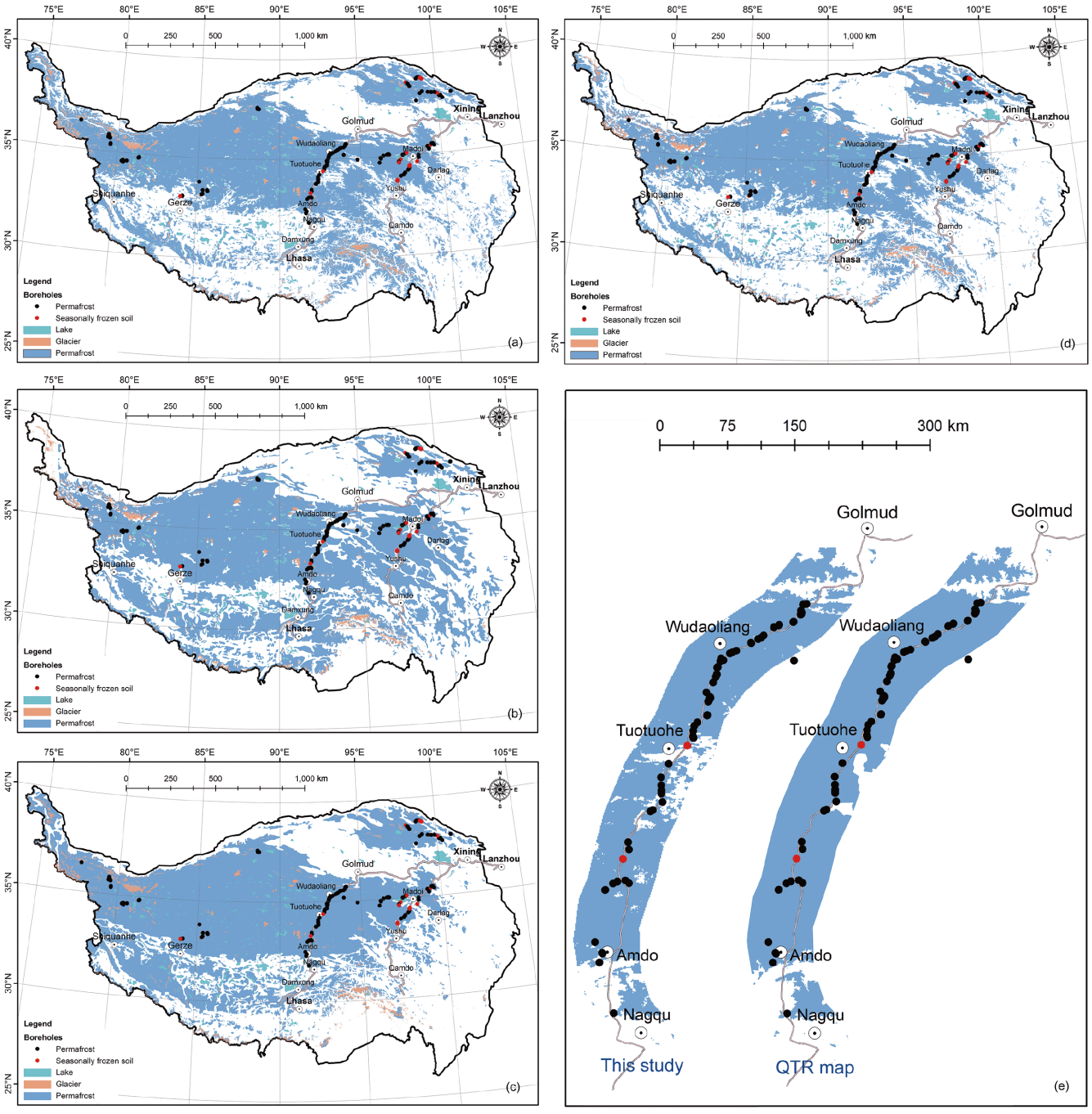

Figure 9 Intercomparisons of permafrost extents among this study (a) and existing maps at the regional scale ((b), Li and Cheng, 1996; (c), Nan et al., 2002; (d), Zou et al., 2017) and the updated permafrost distribution along the Qinghai-Tibet Highway and Railway (e).

3.5 The MALST and SFN criteria for mapping the thermal stability of permafrost

The criteria of MAGT, MAAT and permafrost thickness are defined only to distinguish the different permafrost stability types (Cheng, 1984). As mentioned in Section 2.1, it is very difficult to monitor the MAGT and permafrost thickness, and it is even more difficult to obtain long-term, continuous and spatially dense measurements over a large area. Therefore, the MAAT is typically used as a reference to indicate the occurrence of permafrost (Ran et al., 2015), although it is not an optimal predictor of permafrost thermal stability. Stations where MAAT data are measured are also very sparse in many permafrost areas. Therefore, criteria involving remotely sensed values of MALST and SFN were defined to characterize permafrost thermal stability by comparing the permafrost thermal stability map generated in Section 3.2 with the MALST and SFN values produced using the method

described in Section 2.3.2. The 5th and 95th percentiles are used to define the range of MALST and SFN for each permafrost thermal stability type (Table 4). Table 4 shows that the lower limit of permafrost corresponds to a MALST value of 1.1°C and an SFN value of 0.45. These values can be used to distinguish permafrost from seasonal frost on the TP. The MALST values at the boundaries between stability types are systematically higher than the MAAT criteria shown in Table 1. This systematic difference varies with the stability types being considered. The standard deviation is approximately 2.6°C for the MALST and 0.1 for the SFN, which indicates the spatial differences in this criterion. Referring to the permafrost thermal stability map derived from simulated MAGT (Figure 6), the consistency of the results derived from MALST and SFN using the criteria proposed here is 69.6% and 75.3%, respectively, on the basis of thermal stability type and 90.1% and 91.8%, respectively, on the basis of permafrost extent.

Of course, it is not the best choice to classify permafrost types by using the MALST and SFN criteria proposed here due to the complex relationship between ground temperature and remote sensing-based LST, as mentioned at the beginning of Section 2.2 and in several previous studies (Luo et al., 2018a). However, it should be workable as an alternative areas with little or no data, such as the TP, where the low and sparse vegetation and thin snow cover may have relatively little influence, especially in the western part of the TP. Overall, this criterion improved the ability to use remotely sensed LST data, instead of MAAT data, to monitor permafrost stability on the TP.

4. Discussion

4.1 Total permafrost area on the TP

We summed the reported total areas of permafrost over the TP, which are shown in Table 5. The total areas indicated by several permafrost maps published in the past several decades were recalculated based on the digital version (Ran et al., 2012) and the corresponding ancillary data used in this study, including a map of the distribution of water bodies and glaciers. The differences in the research periods of different studies are ignored based on the assumption that the total area of permafrost over the TP has remained approximately constant over the past 30 years. This assumption holds because there is no direct evidence of permafrost loss except in a few engineering fields over the TP. Comparing these areas with the high-resolution maps produced in recent years by using the empirical frozen soil model, such as the three permafrost maps for the TP (Li and Cheng, 1996; Nan et al., 2002; Zou et al., 2017), it is evident that the differences between them are small. The total areas derived from the map in this study are also similar to those of the new map of permafrost extent (Zou et al., 2017) and predicted results using the improved Noah land surface model (Wu et al., 2018). However, the differences between this study and the permafrost maps covering China produced by Shi (1988) and Qiu et al. (2000) are large. These large differences are mainly derived from the differences in the map scales and classification systems used. First, because areal continuity-based classification systems are used in these maps, the permafrost extent implies the extent of the permafrost region. In other

Table 4 Remote sensing criteria used to identify the permafrost stability types on the Tibetan Plateau

Permafrost stability type	Remotely sensed mean annual land surface temperature (°C)	Remote sensing LST-based surface frost number
Very stable	<−6.0	>0.75
Stable	−3.50 to −6.0	0.64–0.75
Semi-stable	−1.40 to −3.50	0.56–0.64
Transitional	0.30 to −1.40	0.50–0.56
Unstable	1.10–0.30	0.45–0.50

Table 5 Permafrost area over the Tibetan Plateau from various sources[a)]

Map name	Permafrost area ($\times 10^4$ km^2)	Reference
Map of Snow, Ice, and Frozen Ground in China (1:4000000)	154.25	Shi, 1988
Permafrost Map of the Qinghai-Tibet Plateau (1:3000000)	127.19	Li and Cheng, 1996
Map of Geocryological Regionalization and Classification in China (1:10000000)	161.50	Qiu et al., 2000
Map of Glaciers, Frozen Ground and Deserts in China (1:4000000)	122.68	Nan et al., 2002; Wang, 2006
Simulation results using CLM4 for 1980–2000	122.20	Guo et al., 2012
Simulation results using improved Noah model	111.30	Wu et al., 2018
New permafrost extent map in Tibetan Plateau	106.00	Zou et al., 2017
New permafrost stability map over Tibetan Plateau	115.02 (105.47–129.59)*	This study

a) Excluding glaciers and lakes. *, the uncertainty in permafrost area was quantified by using the percentile intervals (PI, 97.5th–2.5th percentile) of ensemble simulated MAGT based on the SVR model with 200 runs.

words, not all of these regions are underlain by permafrost. For example, in terms of the areal fraction or continuity, the map of Qiu et al. (2000) shows that the actual permafrost area on the TP is approximately 129.9×10^4 km^2 (Zhao et al., 2004), which is close to the result of this study. Second, considering only the data and mapping techniques used, the permafrost extents in the existing maps were determined based on the empirical judgment of the authors, except for the maps of Nan et al. (2002) and Zou et al. (2017), and the predicted results of the two empirically based models. However, the mapping of permafrost is heavily dependent on the availability of high-quality data (Heginbottom, 2002). Furthermore, the actual permafrost extent (not the permafrost region) can be more objectively determined by using comprehensive, abundant, and high-quality data, especially remote sensing-based LST measurements and SCD values. Therefore, the small differences between the results of this study and those of other published maps should be more credible, primarily because these maps integrate larger amounts of survey data, and more accurate results can be obtained at higher resolutions (Ran et al., 2012; Ran and Li, 2019).

4.2 Potential applications of the new map

The permafrost stability map proposed in this study is based on more survey data than any previous map covering the TP. It has the potential to support the planning and design of engineering structures for the reduction of permafrost-related hazards and to improve ecosystem management. Thus, it can be used to enhance the social and ecosystem adaptability to the degradation of permafrost. First, degradation of permafrost may lead to reductions in the stability of settlements and mountain slopes (Harris et al., 2001). Thus, engineering planning, optimization, and design in permafrost regions are required to understand the present-day thermal stability of permafrost in different areas. Many studies have shown that the degradation of very stable and stable permafrost may be in the initial stage or a stage of temperature increase, and the thermal inertia of such areas may correspond to tens of thousands of years (Jin et al., 2006). On the other hand, unstable permafrost may be in a stage characterized by a near-zero geothermal gradient and is rapidly thawing upwards (Wu et al., 2010). These permafrost types with different stabilities may require different engineering measures to improve the stability of the substrate and reduce permafrost-related hazards. For very stable and stable permafrost, general engineering measures may be able to mitigate permafrost thawing. However, enhanced measures may be needed for the transitional and unstable permafrost types. For example, within areas of transitional and predominantly unstable permafrost types along the Qinghai-Tibet engineering corridor, a series of proactive roadbed cooling engineering measures have been successfully applied in the design and construction of the Qinghai-Tibet Railway. These measures include solar radiation control by using shading boards, heat convection control using air ducts, thermosyphons and air-cooled embankments, and heat conduction control by using "thermal semiconductor" materials such as crushed rock embankments (Cheng et al., 2008). These enhanced and proactive cooling methods have successfully lowered the ground temperature and the permafrost table under the roadbed of the Qinghai-Tibet Railway and have helped to stabilize the railway (Cheng, 2004, 2005). Second, the permafrost stability map presented in this study, which has better accuracy and resolution than previous products, can be used to support the assessment of water resource vulnerability on the TP. In general, the presence of permafrost increases the complexity of interactions between surface water and groundwater. The type and thermal stability of permafrost are closely related to the availability of water resources (Alessa et al., 2008) and can be used to support a better understanding of the environmental effects of permafrost degradation in a changing world. Additionally, as a baseline, the new dataset, including MAGT and a thermal stability map, can be used to evaluate the permafrost change in the future on the TP.

5. Summary and conclusions

We test the importance ranking of 13 potential predictor variables using the RF technique and found that FDD, TDD, LAI, SCD, elevation, soil moisture, and soil bulk density are the most important factors in the estimation of MAGT. Five statistical learning techniques (GLM, GAM, SVR, RF, and GWR) and their ensemble mean all achieved high accuracy for the prediction of MAGT, but the performance of SVR was similar to that of the ensemble mean of the five models (RMSE=0.75°C, bias=0.01°C, R^2=0.71). Therefore, a new and higher-resolution permafrost stability map covering the TP for the 2010s (2005–2015) was developed with 200 repetitions of the SVR model based on distance-blocked resampling training data from *in situ* MAGT measurements obtained at 237 borehole locations distributed across the TP. Both direct and indirect validations show that the accuracy and reliability of this map are higher than those of previous maps. According to this map, the total area of permafrost on the TP, excluding glaciers and lakes, is approximately 115.02×10^4 km^2. The areas corresponding to the very stable, stable, semi-stable, transitional, and unstable types are 0.86×10^4, 9.62×10^4, 38.45×10^4, 42.29×10^4, and 23.80×10^4 km^2, respectively. The new permafrost stability map is of fundamental importance for supporting engineering planning and design measures intended to reduce permafrost-related hazards and to enhance water resource management. The si-

mulated MAGT and permafrost stability map in this study can be downloaded at https://www.doi.org/10.11888/Geogra.tpdc.270672. A criterion involving remote sensing-based MALST and SFN values was also defined to classify the permafrost stability type, thus providing a basis for the rapid, low-cost, and high-resolution monitoring of permafrost stability on the TP and in other permafrost regions using remote sensing data in the future.

Acknowledgements *This work was supported by the Strategic Priority Research Program of the Chinese Academy of Sciences (Grant No. XDA19070204), and the National Natural Science Foundation of China (Grant Nos. 42071421, 41630856).*

References

Aalto J, Karjalainen O, Hjort J, Luoto M. 2018. Statistical forecasting of current and future circum-arctic ground temperatures and active layer thickness. Geophys Res Lett, 45: 4889–4898

Ackerman S A, Strabala K I, Menzel W P, Frey R A, Moeller C C, Gumley L E. 1998. Discriminating clear sky from clouds with MODIS. J Geophys Res, 103: 32141–32157

Alessa L, Kliskey A, Lammers R, Arp C, White D, Hinzman L, Busey R. 2008. The arctic water resource vulnerability index: An integrated assessment tool for community resilience and vulnerability with respect to freshwater. Environ Manage, 42: 523–541

Breiman L. 2001. Random forests. Mach Learn, 45: 5–32

Brown J, Ferrians Jr O J, Heginbottom J A, Melnikov E S. 1998. Circum-Arctic Map of Permafrost and Ground Ice Conditions. Boulder, CO: National Snow and Ice Data Center/World Data Center for Glaciology. Digit Media

Brunsdon C, Fotheringham S, Charlton M. 1998. Geographically weighted regression. J Roy Stat Soc D-Sta, 47: 431–443

Cao B, Gruber S, Zhang T, Li L, Peng X, Wang K, Zheng L, Shao W, Guo H. 2017. Spatial variability of active layer thickness detected by ground-penetrating radar in the Qilian Mountains, Western China. J Geophys Res-Earth Surf, 122: 574–591

Cheng G D. 1984. Problems on zonation of high-altitude permafrost (in Chinese). Acta Geogr Sin, 39: 185–193

Cheng G. 2004. Influences of local factors on permafrost occurrence and their implications for Qinghai-Xizang Railway design. Sci China Ser D-Earth Sci, 47: 704–709

Cheng G D. 2005. A roadbed cooling approach for the construction of Qinghai-Tibet Railway. Cold Reg Sci Tech, 42: 169–176

Cheng G D, Jin H J. 2013. Permafrost and groundwater on the Qinghai-Tibet Plateau and in northeast China. Hydrogeol J, 21: 5–23

Cheng G D, Sun Z Z, Niu F J. 2008. Application of the roadbed cooling approach in Qinghai-Tibet railway engineering. Cold Reg Sci Tech, 53: 241–258

Cheng G D, Wu T H. 2007. Responses of permafrost to climate change and their environmental significance, Qinghai-Tibet Plateau. J Geophys Res, 112: F02S03

Dorigo W A, Gruber A, De Jeu R A M, Wagner W, Stacke T, Loew A, Albergel C, Brocca L, Chung D, Parinussa R M, Kidd R. 2015. Evaluation of the ESA CCI soil moisture product using ground-based observations. Remote Sens Environ, 162: 380–395

Fang H, Wei S, Jiang C, Scipal K. 2012. Theoretical uncertainty analysis of global MODIS, CYCLOPES, and GLOBCARBON LAI products using a triple collocation method. Remote Sens Environ, 124: 610–621

Florides G, Kalogirou S. 2007. Ground heat exchangers—A review of systems, models and applications. Renew Energy, 32: 2461–2478

Fotheringham A S, Brunsdon C, Charlton M E. 2002. Geographically Weighted Regression: The Analysis of Spatially Varying Relationships. Hoboken: John Wiley & Sons

Garcia D. 2010. Robust smoothing of gridded data in one and higher dimensions with missing values. Comput Stat Data Anal, 54: 1167–1178

Guo D L, Wang H J, Li D. 2012. A projection of permafrost degradation on the Tibetan Plateau during the 21st century. J Geophys Res, 117: D05106

Guo W Q, Liu S Y, Xu J L, Wu L Z, Shangguan D H, Yao X J, Wei J F, Bao W J, Yu P C, Liu Q, Jiang Z L. 2015. The second Chinese glacier inventory: Data, methods and results. J Glaciol, 61: 357–372

Hachem S, Duguay C R, Allard M. 2012. Comparison of MODIS-derived land surface temperatures with ground surface and air temperature measurements in continuous permafrost terrain. Cryosphere, 6: 51–69

Hansson K, Šimůnek J, Mizoguchi M, Lundin L C, van Genuchten M T. 2004. Water flow and heat transport in frozen soil: Numerical solution and freeze-thaw applications. Vadose Zone J, 3: 693–704

Harris S A. 1986. Permafrost distribution, zonation and stability along the Eastern Ranges of the Cordillera of North America. Arctic, 39: 29–38

Harris C, Davies M C R, Etzelmüller B. 2001. The assessment of potential geotechnical hazards associated with mountain permafrost in a warming global climate. Permafrost Periglac Process, 12: 145–156

Harris S A, Brouchkov A, Cheng G D. 2017. Geocryology: Characteristics and Use of Frozen Ground and Permafrost Landforms. Boca Raton (FL): CRC Press

Hastie T J, Tibshirani R J. 1990. Generalized Additive Models (Vol. 43). London: CRC Press

Heginbottom J A. 2002. Permafrost mapping: A review. Prog Phys Geog-Earth Environ, 26: 623–642

Hengl T, Mendes de Jesus J, Heuvelink G B M, Ruiperez Gonzalez M, Kilibarda M, Blagotić A, Shangguan W, Wright M N, Geng X, Bauer-Marschallinger B, Guevara M A, Vargas R, MacMillan R A, Batjes N H, Leenaars J G B, Ribeiro E, Wheeler I, Mantel S, Kempen B. 2017. SoilGrids250m: Global gridded soil information based on machine learning. PLoS ONE, 12: e0169748

Jansson J K, Taş N. 2014. The microbial ecology of permafrost. Nat Rev Microbiol, 12: 414–425

Jin H, Zhao L, Wang S, Jin R. 2006. Thermal regimes and degradation modes of permafrost along the Qinghai-Tibet Highway. Sci China Ser D-Earth Sci, 49: 1170–1183

Karatzoglou A, Meyer D, Hornik K. 2006. Support vector machines in *R*. J Stat Soft, 15: 1–28

Kogan F, Powell A, Fedorov O. 2011. Use of Satellite and *In-Situ* Data to Improve Sustainability. Berlin: Springer

Li J, Sheng Y, Cheng J, Zhang B, Wu J C, Zhang X M. 2011. Characteristics of ground temperatures and influencing factors of permafrost development and distribution in the source region of datong river (in Chinese with English abstract). Prog Geogr, 30: 827–836

Li J, Sheng Y, Wu J C, Feng Z L, Ning Z J, Hu X Y, Zhang X M. 2016. Mapping frozen soil distribution and modeling permafrost stability in the source area of the Yellow River (in Chinese with English abstract). Sci Geogr Sin, 36: 588–596

Li X. 2014. Characterization, controlling, and reduction of uncertainties in the modeling and observation of land-surface systems. Sci China Earth Sci, 57: 80–87

Li X, Cheng G. 1999. A GIS-aided response model of high-altitude permafrost to global change. Sci China Ser D-Earth Sci, 42: 72–79

Li X, Che T, Li X, Wang L, Duan A, Shangguan D, Pan X, Fang M, Bao Q. 2020. CASEarth Poles: Big data for the Three Poles. Bull Am Meteorol Soc, 101: E1475–E1491

Li X, Cheng G D, Jin H J, Kang E S, Che T, Jin R, Wu L Z, Nan Z T, Wang J, Shen Y P. 2008. Cryospheric change in China. Glob Planet Change, 62: 210–218

Li S D, Cheng G D. 1996. Map of Permafrost on the Qinghai-Tibet Plateau (1:3000000) (in Chinese). Lanzhou: Gansu Culture Press

Liaw A, Wiener M. 2002. Classification and regression by randomForest. R News, 2: 18–22

Liu G Y, Wang W, Zhao L, Chen J, Pang Q Q, Wang Z W, Du E J. 2015. Using transient electromagnetic method to sound permafrost depth in the West Kunlun Mountains (in Chinese with English abstract). J Gla-

ciol Geocryol, 37: 38–48
Liu X D, Yin Z Y, Shao X M, Qin N S. 2006. Temporal trends and variability of daily maximum and minimum, extreme temperature events, and growing season length over the eastern and central Tibetan Plateau during 1961–2003. J Geophys Res, 111: D19109
Luo D, Jin H, Jin X, He R, Li X, Muskett R R, Marchenko S S, Romanovsky V E. 2018b. Elevation-dependent thermal regime and dynamics of frozen ground in the Bayan Har Mountains, northeastern Qinghai-Tibet Plateau, southwest China. Permafrost Periglac Process, 29: 257–270
Luo D, Liu L, Jin H, Wang X, Chen F. 2020. Characteristics of ground surface temperature at Chalaping in the Source Area of the Yellow River, northeastern Tibetan Plateau. Agric For Meteorol, 281: 107819
Luo D, Jin H, Marchenko S S, Romanovsky V E. 2018a. Difference between near-surface air, land surface and ground surface temperatures and their influences on the frozen ground on the Qinghai-Tibet Plateau. Geoderma, 312: 74–85
McColl K A, Vogelzang J, Konings A G, Entekhabi D, Piles M, Stoffelen A. 2014. Extended triple collocation: Estimating errors and correlation coefficients with respect to an unknown target. Geophys Res Lett, 41: 6229–6236
McCullagh P, Nelder J. 1989. Generalized Linear Models (Vol. 37). London: CRS Press
McCune B, Keon D. 2002. Equations for potential annual direct incident radiation and heat load. J Veg Sci, 13: 603–606
Mitchell T D, Jones P D. 2005. An improved method of constructing a database of monthly climate observations and associated high-resolution grids. Int J Climatol, 25: 693–712
Nan Z T, Li S X, Liu Y Z. 2002. Mean annual ground temperature distribution on the Tibetan Plateau: Permafrost distribution mapping and further application (in Chinese with English abstract). J Glaciol Geocryol, 24: 142–148
Nan Z T, Gao Z S, Li S X, Wu T H. 2003. Permafrost changes in the northern limit of permafrost on the Qinghai-Tibet Plateau in the last 30 years (in Chinese with English abstract). Acta Geogr Sin, 58: 817–823
Nan Z T, Huang P P, Zhao L, 2013. Permafrost distribution modeling and depth estimation in the Western Qinghai-Tibet Plateau (in Chinese with English abstract). Acta Geogr Sin, 68: 318–327
Nelson F E, Outcalt S I. 1987. A computational method for prediction and regionalization of permafrost. Arct Alp Res, 19: 279–288
Obu J, Westermann S, Bartsch A, Berdnikov N, Christiansen H H, Dashtseren A, Delaloye R, Elberling B, Etzelmüller B, Kholodov A, Khomutov A, Kääb A, Leibman M O, Lewkowicz A G, Panda S K, Romanovsky V, Way R G, Westergaard-Nielsen A, Wu T, Yamkhin J, Zou D. 2019. Northern Hemisphere permafrost map based on TTOP modelling for 2000–2016 at 1 km^2 scale. Earth-Sci Rev, 193: 299–316
Pepin N, Bradley R S, Diaz H F, Baraër M, Caceres E B, Forsythe N, Fowler H, Greenwood G, Hashmi M Z, Liu X D, Miller J R, Ning L, Ohmura A, Palazzi E, Rangwala I, Schöner W, Severskiy I, Shahgedanova M, Wang M B, Williamson S N, Yang D Q. 2015. Elevation-dependent warming in mountain regions of the world. Nat Clim Change, 5: 424–430
Péwé T L. 1983. Alpine permafrost in the contiguous United States: A review. Arct Alp Res, 15: 145–156
Qiao Y P, Zhao L, Pang Q Q, Chen J, Zou D F, Gao D S. 2015. Characteristics of permafrost in Gerze County on the Tibetan plateau (in Chinese with English abstract). J Glaciol Geocryol, 37: 1453–1460
Qin Y, Wu T, Zhao L, Wu X, Li R, Xie C, Pang Q, Hu G, Qiao Y, Zhao G, Liu G, Zhu X, Hao J. 2017. Numerical modeling of the active layer thickness and permafrost thermal state across Qinghai-Tibetan plateau. J Geophys Res-Atmos, 122: 11604–11620
Qiu G Q, Zhou Y W, Guo D X, Wang Y X. 2000. The Map of Geocryological Regionalization and Classification in China (in Chinese). Beijing: Science Press
Ran Y H, Li X, Cheng G D, Zhang T J, Wu Q B, Jin H J, Jin R. 2012. Distribution of permafrost in China: An overview of existing permafrost maps. Permafrost Periglac Process, 23: 322–333
Ran Y H, Li X, Cheng G. 2018. Climate warming over the past half century has led to thermal degradation of permafrost on the Qinghai-Tibet Plateau. Cryosphere, 12: 595–608
Ran Y H, Li X, Jin R, Guo J. 2015. Remote sensing of the mean annual surface temperature and surface frost number for mapping permafrost in China. Arctic Antarctic Alpine Res, 47: 255–265
Ran Y H, Li X. 2019. Progress, Challenges and opportunities of permafrost mapping in China (in Chinese with English abstract). Adv Earth Sci, 34: 1015–1027
Romanovsky V E, Smith S L, Christiansen H H. 2010. Permafrost thermal state in the polar Northern Hemisphere during the international polar year 2007–2009: A synthesis. Permafrost Periglac Process, 21: 106–116
Sandri M, Zuccolotto P. 2006. Variable selection using random forests. In: Zani S, Cerioli A, Riani M, Vichi M, eds. Data Analysis, Classification and the Forward Search. Berlin, Heidelberg: Springer
Schuur E A G, McGuire A D, Schädel C, Grosse G, Harden J W, Hayes D J, Hugelius G, Koven C D, Kuhry P, Lawrence D M, Natali S M, Olefeldt D, Romanovsky V E, Schaefer K, Turetsky M R, Treat C C, Vonk J E. 2015. Climate change and the permafrost carbon feedback. Nature, 520: 171–179
Shi Y F. 1988. Map of Snow, Ice and Frozen Ground in China (1:4000000) (in Chinese). Beijing: Cartographic Publishing House
Shen Y, Zhao P, Pan Y, Yu J. 2014. A high spatiotemporal gauge-satellite merged precipitation analysis over China. J Geophys Res-Atmos, 119: 3063–3075
Sheng Y, Li J, Wu J C, Ye B S, Wang J. 2010. Distribution patterns of permafrost in the upper area of Shule River with the application of GIS technique. J China Univ Mining Tech, 39: 32–39
Shi C X, Xie Z H, Qian H, Liang M L, Yang X C. 2011. China land soil moisture EnKF data assimilation based on satellite remote sensing data. Sci China Earth Sci, 54: 1430–1440
Sun Z Z, Ma W, Dang H M, Yun H B, Wu G L. 2013. Characteristics and causes of embankment deformation for Qinghai-Tibet Railway in permafrost regions (in Chinese with English abstract). Rock Soil Mechan, 34: 2667–2671
Tang Z, Wang J, Li H, Yan L. 2013. Spatiotemporal changes of snow cover over the Tibetan plateau based on cloud-removed moderate resolution imaging spectroradiometer fractional snow cover product from 2001 to 2011. J Appl Remote Sens, 7: 073582
Vapnik V. 1995. The Nature of Statistical Learning Theory. New York: Springer
Wan Z, Zhang Y, Zhang Q, Li Z L. 2004. Quality assessment and validation of the MODIS global land surface temperature. Int J Remote Sens, 25: 261–274
Wang T. 2006. Map of the Glaciers, Frozen Ground and Desert in China (1:4000000) (in Chinese). Beijing: SinoMaps Press
Wang Q F, Zhang T J, Wu J C, Peng X Q, Zhong X Y, Mou C, Cheng G D. 2013. Investigation on permafrost distribution over the upper reaches of the Heihe River in the Qilian Mountains (in Chinese with English abstract). J Glaciol Geocryol, 35: 19–25
Wood S N. 2011. Fast stable restricted maximum likelihood and marginal likelihood estimation of semiparametric generalized linear models. J R Statistical Soc-Ser B Statisti Methodol, 73: 3–36
Wu Q B, Zhang T J. 2008. Recent permafrost warming on the Qinghai-Tibetan Plateau. J Geophys Res, 113: D13108
Wu Q, Hou Y, Yun H, Liu Y. 2015. Changes in active-layer thickness and near-surface permafrost between 2002 and 2012 in alpine ecosystems, Qinghai-Xizang (Tibet) Plateau, China. Glob Planet Change, 124: 149–155
Wu J C, Sheng Y, Wu Q B, Wen Z. 2010. Processes and modes of permafrost degradation on the Qinghai-Tibet Plateau. Sci China Earth Sci, 53: 150–158
Wu J, Yu S, Yu H, Li J. 2007. Permafrost in the middleeast section of Qilian Mountains (II): Characters of permafrost (in Chinese with English abstract). J Glaciol Geocryol, 29: 426–432
Wu X, Nan Z, Zhao S, Zhao L, Cheng G. 2018. Spatial modeling of permafrost distribution and properties on the Qinghai-Tibet Plateau.

Permafrost Periglac Process, 29: 86–99
Xiang Y, Xiao Z Q, Ling S L, Wang J D, Song J L. 2014. Validation of global land surface satellite (GLASS) leaf area index product. Int J Remote Sens, 18: 573–584
Xiao Z, Liang S, Wang J, Chen P, Yin X, Zhang L, Song J. 2014. Use of general regression neural networks for generating the GLASS leaf area index product from time-series MODIS surface reflectance. IEEE Trans Geosci Remote Sens, 52: 209–223
Yang M X, Nelson F E, Shiklomanov N I, Guo D L, Wan G N. 2010. Permafrost degradation and its environmental effects on the Tibetan Plateau: A review of recent research. Earth-Sci Rev, 103: 31–44
Yao T D, Thompson L G, Mosbrugger V, Zhang F, Ma Y M, Luo T X, Xu B Q, Yang X X, Joswiak D R, Wang W C, Joswiak M E, Devkota L P, Tayal S, Jilani R, Fayziev R. 2012. Third pole environment (TPE). Environ Dev, 3: 52–64
Ye H C, Ladochy S, Yang D Q, Zhang T J, Zhang X B, Ellison M. 2004. The impact of climatic conditions on seasonal river discharges in Siberia. J Hydrometeor, 5: 286–295
Yu H, Wu Q B, Liu Y Z. 2008. The long-term monitoring system on permafrost regions along the Qinghai-Tibet Railway (in Chinese with English abstract). J Glaciol Geocryol, 30: 475–481
Zhang T J. 2005. Influence of the seasonal snow cover on the ground thermal regime: An overview. Rev Geophys, 43: RG4002
Zhang X M, Nan Z T, Wu J C, Du E J, Wang T, You Y H. 2011. Modeling permafrost distribution in Wenquan area over Qinghai-Tibet Plateau by using multivariate adaptive regression splines (in Chinese with English abstract). J Glaciol Geocryol, 33: 1088–1097
Zhao L, Cheng G D, Ding Y J. 2004. Studies on frozen ground of China. J Geogr Sci, 14: 411–416
Zou D F, Zhao L, Sheng Y, Chen J, Hu G J, Wu T H, Wu J C, Xie C W, Wu X D, Pang Q Q, Wang W, Du E J, Li W P, Liu G Y, Li J, Qin Y H, Qiao Y P, Wang Z W, Shi J Z, Cheng G D. 2017. A new map of permafrost distribution on the Tibetan Plateau. Cryosphere, 11: 2527–2542
Zwieback S, Scipal K, Dorigo W, Wagner W. 2012. Structural and statistical properties of the collocation technique for error characterization. Nonlin Processes Geophys, 19: 69–80

(Responsible editor: Jiancheng SHI)